Magnetically activatable insect viral vectors promote anticancer immunity through spatially confined gene disruption

Xiaoyue Yang[1], Laura Tong[2], Yidan Pan[3], Jin Huang[1], Zhongchao Yi[1], Daheng He[4], Jingpeng Liu[4], Chi Wang[4], Ying Liang[5], Sheng Tong[1,]*

[1] F. Joseph Halcomb III, M.D. Department of Biomedical Engineering, University of Kentucky, Lexington, Kentucky 40536, USA

[2] Department of Bioengineering, Stanford University, Stanford, California 94305, USA

[3] Department of Genetics, The University of Texas MD Anderson Cancer Center, Houston, Texas 77030, USA

[4] Division of Cancer Biostatistics, Department of Internal Medicine, University of Kentucky, Lexington, Kentucky 40536, USA

[5] New York Blood Center, New York, New York 10065, USA

[*] Correspondence: Sheng Tong, sheng.tong@uky.edu

ABSTRACT

Immune checkpoint blockade can elicit durable antitumor responses, yet tumor immune heterogeneity and adaptive resistance often necessitate combination strategies that may cause systemic toxicity. Here we develop a magnetically activatable nanosystem that integrates a non-replicating insect viral vector with magnetic nanoparticles (MBV) to enable spatially confined genome editing within tumors. Magnetic activation functions as a physical on-switch that restores viral entry under complement pressure, enabling localized CRISPR-mediated disruption of immune checkpoints. Concurrently, baculoviral transduction engages antiviral programs, reshaping the tumor immune microenvironment. In a syngeneic colon cancer model, MBV-mediated disruption of *Pdl1* confines checkpoint loss to tumor tissue while preserving virus-induced immune activation, resulting in increased immune infiltration and tumor growth suppression. MBV-*Pdl1* further synergizes with systemic CTLA-4 blockade, extending survival without overt toxicity. These results establish MBV as a controllable genome-editing platform that couples magnetic precision with virus-encoded immune priming to enable localized, combination immunomodulation in solid tumors.

Cancer progression is enabled in part by active evasion of immune surveillance through upregulation of inhibitory checkpoints that restrain effector immune responses [1, 2]. This insight has motivated the development of immune-checkpoint inhibitors (ICIs), most prominently antibodies targeting the PD-1/PD-L1 and CTLA-4 pathways, which can induce durable responses in subsets of patients [3, 4]. However, the majority of tumors exhibit intrinsic or acquired resistance to single-agent checkpoint blockade, reflecting heterogeneity of immune suppression and adaptive engagement of compensatory inhibitory pathways within the tumor microenvironment [5, 6]. Combination immunotherapies can partially overcome these barriers [7, 8, 9, 10], but their clinical implementation is constrained by systemic toxicity, mismatched pharmacokinetics, and limited spatiotemporal control over immune modulation [11].

Genome-editing offers an alternative strategy for immune modulation by enabling direct disruption of immune regulatory genes within tumor tissue [12, 13, 14]. CRISPR-Cas9 systems allow rapid, programmable targeting of endogenous loci and support multiplexed interventions across parallel pathways [15, 16, 17]. Compared with antibody-based inhibition, genomic disruption can provide durable suppression of adaptive resistance mechanisms. Nonetheless, therapeutic gene editing remains limited by insufficient spatial and temporal control, off-target activities, and systemic dissemination of delivery vectors [18, 19, 20, 21]. Viral delivery platforms, including adeno-associated viruses (AAVs) and lentiviral vectors, can persist in vivo and disseminate beyond target sites, increasing the risk of long-term adverse events and restricting clinical use to ex vivo or anatomically confined applications [18, 22, 23].

Baculovirus (Autographa californica multiple nucleopolyhedrovirus, AcMNPV) is an insect virus that cannot replicate in mammalian cells [24]. Nonetheless, baculovirus efficiently transduces a broad range of mammalian cell types through its envelope glycoprotein gp64, which is thought to have originated from an ancestral thogotovirus [25, 26, 27, 28]. Baculovirus transduction proceeds through electrostatic binding of gp64 to heparin sulfate proteoglycans on the cell surface, gp64-mediated pH-dependent membrane fusion

to enable endosomal escape [29], and nuclear translocation driven by the capsid protein P78/83 that promotes actin polymerization [30], ultimately leading to ejection of the viral genome through the nuclear pore complex [31]. Baculovirus supports large DNA payloads (> 38kb) and transient transgene expression, features advantageous for genome editing. However, in vivo administration of baculovirus results in rapid complement-mediated neutralization via both classical and alternative pathways, which has limited its use as a gene-delivery vector [32].

We previously demonstrated that conjugation of baculovirus with magnetic nanoparticles (MNPs) enables spatially confined activation under an external magnetic field [33]. Magnetic field enriches viral vectors on the cell surface, enhances cell entry, and promotes nuclear transport via enhanced actin polymerization. Collectively, magnetic activation and complement neutralization function as orthogonal on- and off-switches for in vivo gene delivery. In parallel, the baculovirus genome is enriched in CpG motifs that activate innate immune pathways, including Toll-like receptor 9 signaling, eliciting interferon response and antigen-presentation programs [34, 35]. These properties suggest an opportunity to couple spatially controlled genome editing with virus-induced immune activation.

Here we develop magnetically activatable baculoviral vectors (MBVs) to achieve localized disruption of immune checkpoints within tumors (Fig. 1). We focus on *Pdl1*, a checkpoint gene commonly upregulated in response to interferon signaling and viral infection and across many cancer types [36, 37, 38], and evaluate MBV-*Pdl1* in a syngeneic colon cancer model with limited responsiveness to PD-L1 antibody blockade [39]. We show that magnetic activation enables spatially confined *Pdl1* disruption without detectable off-target editing in normal tissues. Beyond checkpoint disruption, MBV transduction induces chemokine signaling, antigen-presentation pathways, and interferon responses that reshape the tumor immune microenvironment. Together, these effects promote immune infiltration and effector activation, resulting in tumor growth suppression and prolonged survival. Our results establish MBV as a controllable genome-

editing platform that integrates magnetic precision with virus-induced immune priming to enable localized, combination immunomodulation in solid tumors.

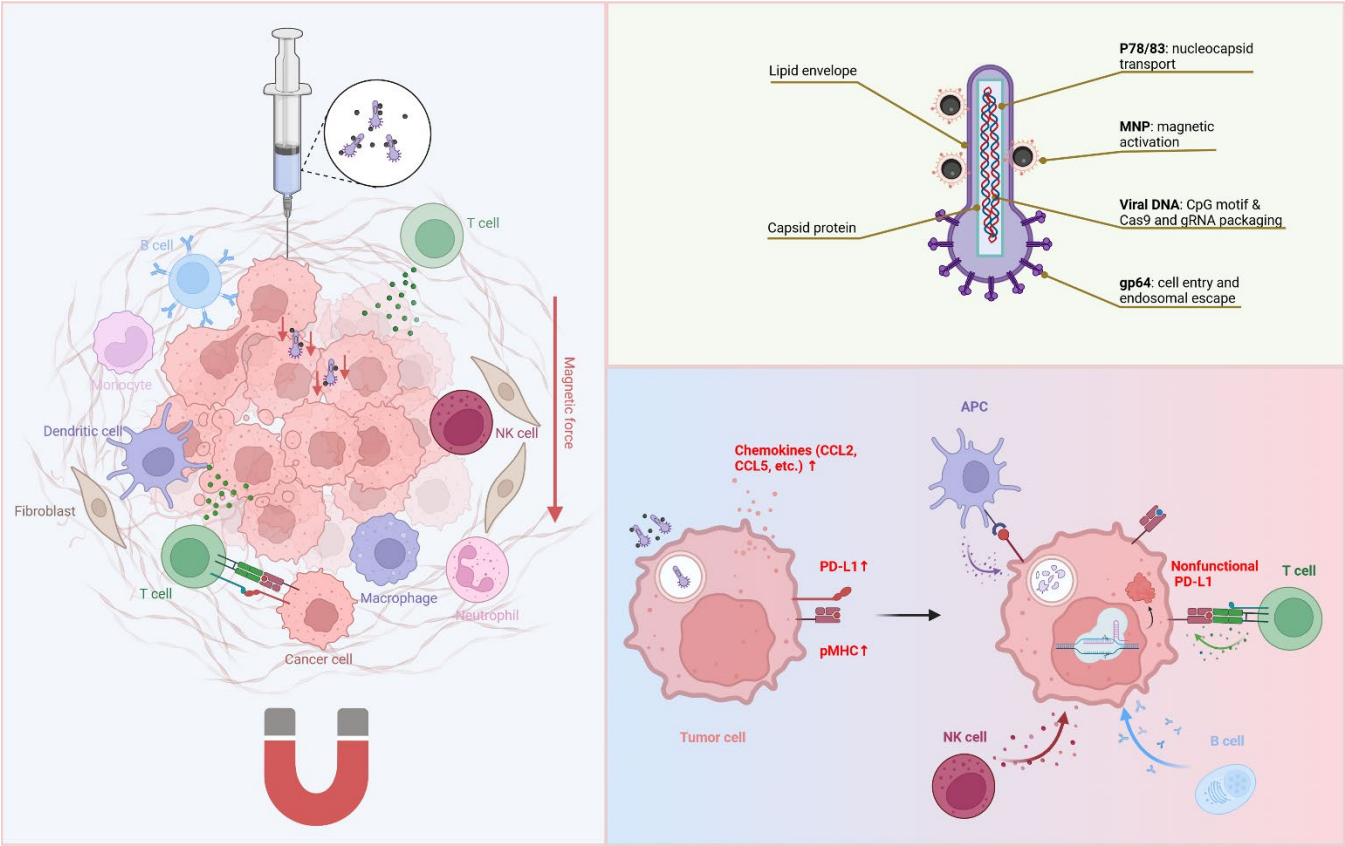

Fig. 1 Schematic of MBV-mediated anticancer immunity. **a**. MBVs are administered via intratumoral infusion followed by brief magnetic activation, Magnetic activation enhances MBV cellular entry under complement pressure and subsequently induces antiviral responses and *Pdl1* disruption, which together shape a localized anticancer immune response. MBVs that escape into the systemic circulation are inhibited by the complement system, thereby limiting off-target exposure. **b**. Schematic of key functional elements of MBV enabling localized gene disruption and immune modulation. **c**. MBV-induced immune events include increased chemokine release that promote lymphocyte infiltration, enhanced antigen presentation, and disruption of *Pdl1,* thereby relieving inhibitory signaling on infiltrating effector cells.

Synthesis and characterization of MBV

MBV was generated by electrostatic conjugation of MNPs to the surface of baculoviral vectors (BVs). MNPs functionalized with TAT peptides were synthesized using a two-step procedure that enabled control over particle size, dispersity, and peptide density (Fig. 2a, Supplementary Fig. S1) [40]. The cationic TAT

peptides facilitated binding to the negatively charged baculoviral envelope. BV vectors encoding SpCas9, reporters, and gRNAs were constructed within a single viral genome, leveraging the large cargo capacity of BV to improve editing efficiency and reduce production complexity (Supporting Fig. S2). MBV complexes were assembled by mixing MNPs with BV at a ratio of ~3 μg Fe per 10^7 pfu for 10 min in PBS (Fig. 2a), a condition optimized to preserve gp64-mediated endosomal escape while ensuring stable nanoparticle association.

BV transduction efficiency was first evaluated in MC38 murine colon adenocarcinoma cells, the cell line used to establish the syngeneic tumor model. More than 50 % of cells expressed eGFP at a multiplicity of infection (MOI) of 5 (Fig. 2b). eGFP expression peaked at 24 h and declined to undetectable levels by day 7 (Fig. 2c), consistent with transient BV-mediated transgene expression.

To assess complement inhibition and magnetic activation as functional off- and on-switches in MC38 cells, BV transduction was evaluated in the presence of 50% adult mouse serum (AMS) (Fig. 2d, Supplementary Fig. S3). AMS markedly reduced both the fraction of eGFP-positive cells and expression intensity (Fig. 2e). In contrast, magnetic activation of MBV restored robust transduction under complement pressure, yielding higher expression levels than BV in AMS-free conditions. Flow cytometry showed ~80% inhibition of BV transduction by AMS, whereas magnetically activated MBV fully rescues transgene expression (Fig. 2f, g). These results confirm that complement sensitivity suppresses off-target BV activity, while magnetic activation enables localized gene delivery.

The murine *Pdl1* locus comprises five exons on chromosome 19. Six candidate guide RNAs targeting early exons or key structural regions were designed and screened in MC38 cells (Supplementary Table S1) [41]. Based on T7E1 cleavage and next generation sequencing (NGS) analysis, a guide targeting exon 3 was selected (Fig. 2h, i, Supplementary Fig. S4). NGS revealed that ~87% of Cas9-induced indels were frameshift mutations, indicating efficient functional disruption (Fig. 2j).

BV transduction increased PD-L1 expression in MC38 cells in a transduction-dependent manner, consistent with interferon-mediated checkpoint induction (Fig. 2k) [36]. In contrast, BV-*Pdl1* reduced PD-L1 expression at matched MOIs without inducing high cytotoxicity (Fig. 2l, Supplementary Fig. S5). MBV-*Pdl1* achieved higher disruption efficiency than BV-*Pdl1* (Supplementary Fig. S6). AMS suppressed both eGFP expression and *Pdl1* disruption by BV-*Pdl1*, whereas magnetic activation of MBV-*Pdl1* partially restored editing activity (Fig. 2m, n), demonstrating magnetically controlled CRISPR activity under complement pressure.

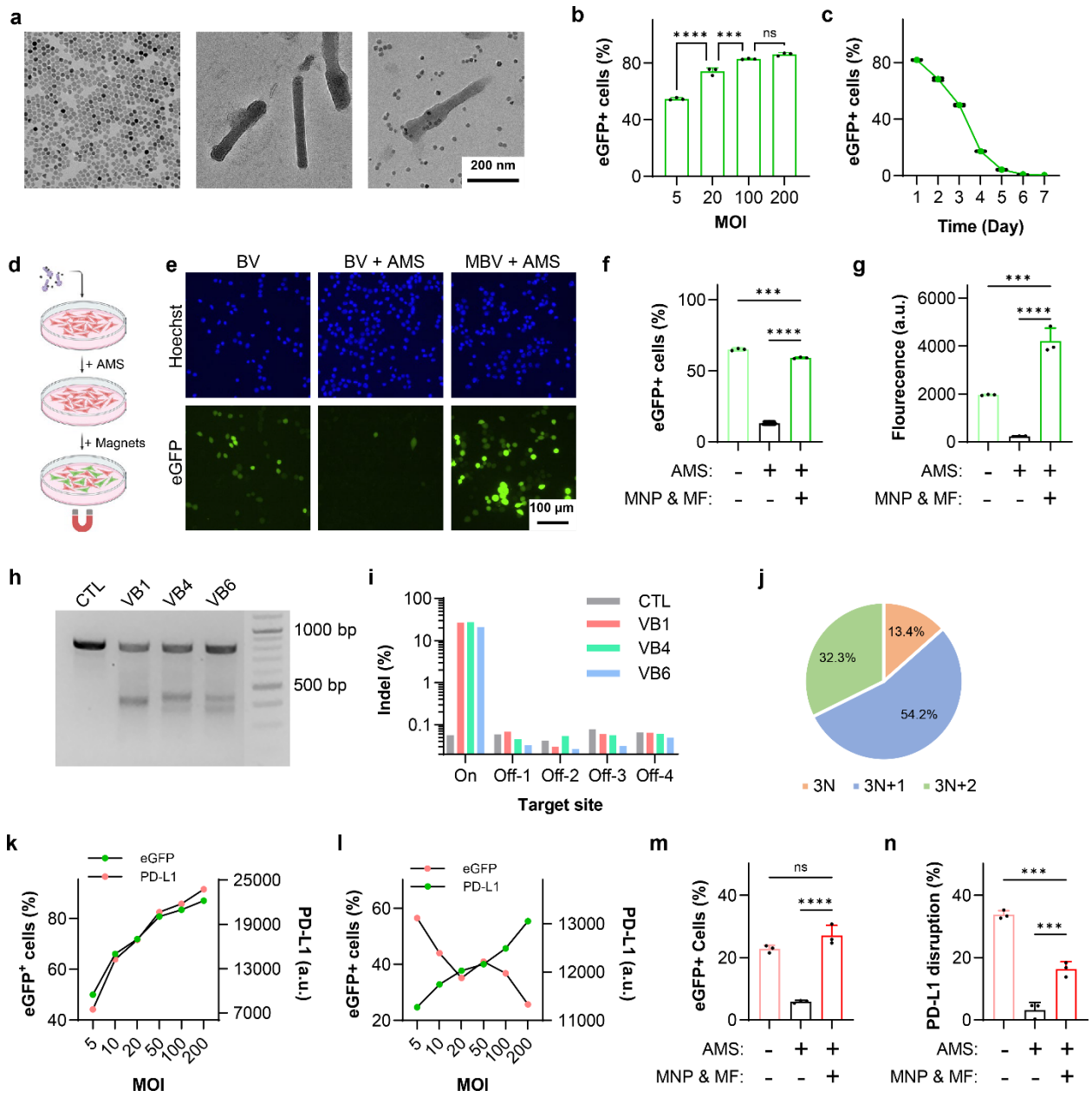

Fig. 2 Characterization of MBV. **a**. Transmission electron microscopy images of magnetic nanoparticles (MNPs), baculovirus (BV), and magnetically modified baculovirus (MBV). Samples in the two right panels were negatively stained with phosphotungstic acid. **b**, **c**. Efficiency and temporal profile of BV transduction in MC38 cells. **d.** Schematic of the in vitro assay used to evaluate magnetic activation of MBV-eGFP under complement pressure. **e**. Representative fluorescence microscopy images of MC38 cells incubated with BV-eGFP alone, BV-eGFP in the presence of adult mouse serum (AMS), and MBV-eGFP with AMS and magnetic activation. **f**, **g**. Flow cytometry analysis of AMS-mediated inhibition and magnetic activation of BV-eGFP-driven eGFP expression. **h**. T7 endonuclease I (T7E1) analysis of three candidate guide RNAs (gRNAs; VB1, VB4, and VB6) targeting exon 3. **i**. Evaluation of on- and off-target activities of the three candidate gRNAs by next generation sequencing (NGS). Data represent the mean of three technical replicates. **j**. Distribution of VB1-induced insertion

and deletion (Indel) events categorized by resulting reading-frame shifts, quantified by NGS. **k**, **l.** Flow cytometry analysis of eGFP and PD-L1 expression in MC38 cells following transduction by BV-eGFP and BV-*Pdl1*-eGFP, respectively. **m**, **n**. Flow cytometry analysis of AMS inhibition and magnetic activation of BV-*Pdl1*-eGFP-mediated eGFP expression and PD-L1 disruption in MC38 cells. Data are presented as mean ± s.d. ns, ***, and **** denote no significance, $P < 0.001$, and $P < 0.0001$, respectively.

BV transduction induces immune-associated signaling in vitro

To isolate immune effects attributable to BV transduction independent of *Pdl1* disruption, a control vector encoding Cas9 without a targeting guide RNA (BV-Cas9) was generated. Similar to BV-eGFP, BV-Cas9 increased PD-L1 expression relative to untreated cells, whereas BV-*Pdl1* disrupted PD-L1 expression in 45.5% of cells (Supplementary Fig. S7).

Transcriptomic profiling of MC38 cells treated with BV-*Pdl1*, MBV-Cas9, and MBV-*Pdl1* was performed using the nCounter® Tumor Signaling 360 Panel. Both BV-*Pdl1* and MBV-*Pdl1* reduced *Pdl1* transcript level (Fig. 3a). In contrast, global transcriptional changes were largely shared across all treated groups and distinct from untreated controls, indicating that BV transduction was the dominant driver of immune-related gene expression (Fig. 3b, c).

BV-treated cells exhibited marked upregulation of chemokines associated with lymphocyte recruitment, including *Ccl2*, *Cxcl11*, *Cxcl10*, *Ccl5* (Fig. 3d, Supplementary Fig. S8a, c). Gene-set analysis revealed activation of chemokine signaling, antigen processing and presentation, and interferon response pathways (Fig. 3e, Supplementary Fig. S8b, d), consistent with a coordinated antiviral response.

To evaluate downstream immune activation, BV-transduced MC38 cells were cocultured with bone marrow-derived dendritic cells (BMDCs). Coculture induced upregulation of canonical maturation markers (*Cd86*, *Cd40*, *Il-12*, *Tnf-α*, *Ifn-α1*, and *Ifn-β1*), indicating dendritic cell activation (Fig. 3f). When cocultured with splenocytes, BV-*Pdl1*-treated MC38 cells elicited greater cytotoxicity than BV-Cas9-treated cells (Fig. 3g). Correspondingly, splenocytes exposed to BV-*Pdl1*-treated cells exhibited elevated

expression of cytotoxic effector genes, including *Gzmb*, *Ifn-γ*, relative to BV-Cas9 (Fig. 3h). Therefore, disruption of *Pdl1* mitigates compensatory checkpoint upregulation associated with antiviral responses, thereby coupling immune recruitment with checkpoint inhibition to enhance cytotoxic effector activity.

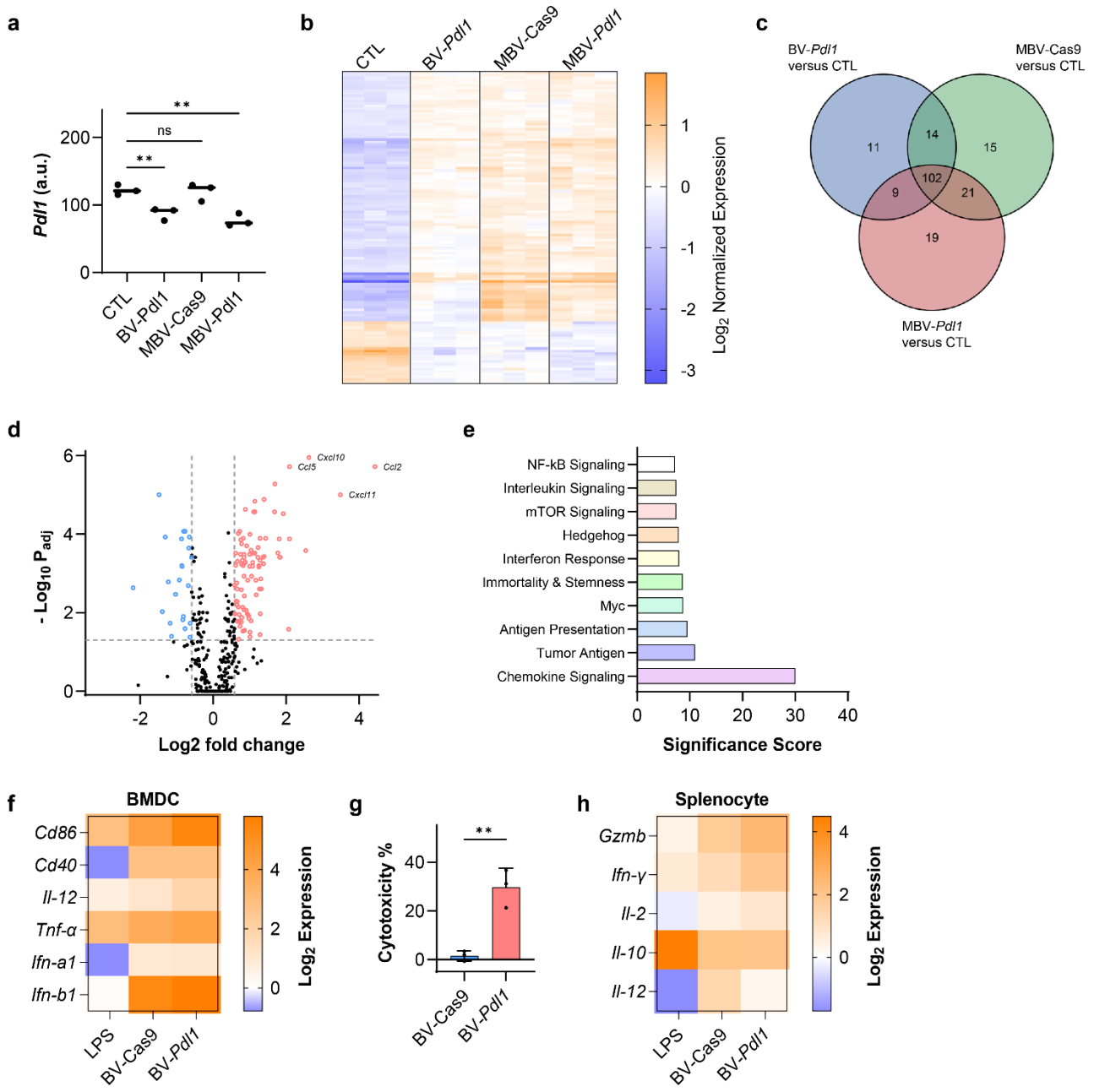

Fig 3. BV-*Pdl1* enhances anticancer immunity through coordinated antiviral responses and *Pdl1* disruption. Transcriptomic responses of MC38 cells treated with BV-*Pdl1*, MBV-Cas9, and MBV-*Pdl1* were analyzed using the nCounter® Tumor Signaling 360 Panel. **a**. *Pdl1* expression in MC38 cells following the indicated treatments. ns and ** denote

no significance and $P < 0.01$, respectively. **b**. Heat map of normalized gene expression across treatment groups. n = 3 per group. **c**. Venn diagram of differentially expressed genes ($|\log_2 FC| \geq 1$, $P_{adj} < 0.05$) in BV-*Pdl1*-, MBV-Cas9-, MBV-*Pdl1*-treated cells relative to untreated controls. **d**. Differential gene expression in MC38 cells treated with MBV-*Pdl1* relative to PBS control. *P* values were adjusted using the Benjamini and Yekutieli method for multiple testing correction. **e**. Pathway enrichment analysis of MBV-*Pdl1*-treated MC38 cells relative to PBS control. Bone marrow-derived dendritic cells (BMDCs) were cocultured with BV-*Pdl1*-treated MC38 cells. **f**. Gene expression in BMDCs quantified by RT-qPCR and normalized to coculture with untreated MC38 cells. Lipopolysaccharide (LPS) treatment were used as a positive control (n = 3 per group). Splenocytes were cocultured with BV-*Pdl1*-treated MC38 cells. **g**. Splenocytes-mediated cytotoxicity against BV-transduced MC38 cells relative to untreated control. Data are presented as mean ± s.d. ** denotes $P < 0.01$. **h**. Gene expression in splenocytes quantified by RT-qPCR and normalized to coculture with untreated MC38 cells. LPS treatment were used as a positive control (n = 3 per group).

Intratumoral activation of MBV-*Pdl1* suppresses tumor growth

To evaluate the effect of localized *Pdl1* disruption in vivo, C57BL/6 mice bearing established MC38 tumors (~50 mm^3) were treated by intratumoral infusion of MBV-*Pdl1* followed by magnetic activation (Fig. 4a). A custom magnetic array composed of four cylindrical NdFeB magnets arranged in alternating polarity was integrated into a 3D-printed animal bed to ensure reproducible tumor positioning (Fig. 4b, Supplementary Fig. S9). Mice were maintained under anesthesia with the tumor aligned within the magnetic field for 1 h after each infusion. Simulated magnetic flux density and force distribution at the tumor surface were comparable to in vitro activation conditions (Fig. 4c, d, Supplementary Fig. S10).

Magnetic nanoparticles enabled noninvasive tracking of MBV distribution by T_2-weighted MRI (Supplementary Fig. S11). MRI imaging and histological analysis revealed localized accumulation of MBV primarily surrounding the injection track (Fig. 4e, f), similar to other locally administered large nanoparticles [42]. To quantify intratumoral transduction, tumor treated with MBV-eGFP were divided into four fragments and analyzed by flow cytometry. $eGFP^+$ cells ranged from 0.6% to 2.7% across fragments, reflecting heterogeneous intratumoral distribution (Fig. 4g). The majority of $eGFP^+$ cells were $CD44^+$ tumor cells with lower levels detected in ER-TR^+ fibroblasts, and $CD45^+$ immune cells (Fig. 4h). It should be noted that BV has low transduction efficiency in cells of hematopoietic origin [43]. The eGFP signals in

$CD45^+$ cells likely reflect the rapid clearance of MBV transduced tumor cells. No eGFP expression was detected in major organs, indicating spatial confinement of transgene expression (Fig. 4i). Localized BV transduction was confirmed by ex vivo fluorescence imaging of excised tumors and major organs (Supplementary Fig. S12). Next-generation sequencing confirmed *Pdl1* indels in tumors but not in distal organs following MBV-*Pdl1* treatment (Fig. 4j, k).

Therapeutic efficacy was evaluated by comparing PBS, MNP alone, BV-*Pdl1*, MBV-*Pdl1*, and systemic anti-PD-L1 antibody (aPD-L1). MBV- *Pdl1* was administered every three days for four doses to account for heterogeneous intratumoral distribution and transient transgene expression (Fig. 4a). MBV-*Pdl1* produced the strongest tumor growth suppression among all groups, including aPD-L1, whereas MNP or BV-*Pdl1* alone induced only modest delay (Fig. 4l). MBV-*Pdl1* significantly prolonged survival, with a median survival of 18 days compared with 10 days for PBS and 12 days for aPD-L1 (Fig. 4m). No significant body weight loss was observed (Supplementary Fig. 13).

Dose escalation of MBV-*Pdl1* did not further improve survival relative to standard dosing but remained superior to MBV-eGFP (Supplementary Fig. S14). Tumors derived from MC38 PD-L1 knockout cells exhibited only marginally reduced growth compared with wild-type tumors (Supplementary Fig. S15), indicating that tumor-intrinsic PD-L1 loss alone is insufficient to account for the observed therapeutic effect.

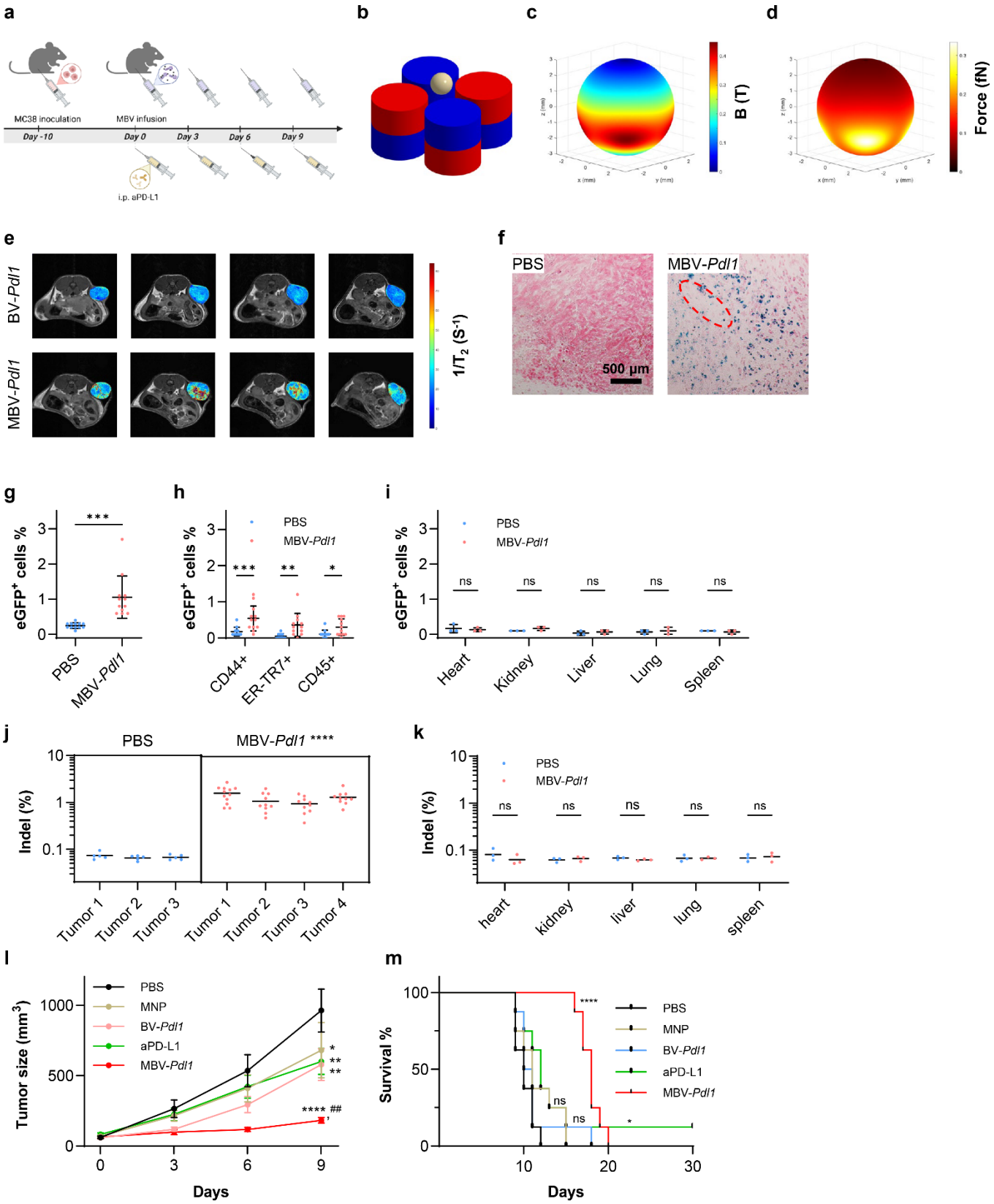
a
MC38 inoculation
MBV infusion
Day -10
Day 0
Day 3
Day 6
Day 9
i.p. aPD-L1
b
c
B (T)
d
Force (fN)
e
BV-Pdl1
MBV-Pdl1
1/T2 (S-1)
f
PBS
MBV-Pdl1
500 μm
g
eGFP+ cells %
***
PBS
MBV-Pdl1
h
eGFP+ cells %
PBS
MBV-Pdl1
***
**
*
CD44+
ER-TR7+
CD45+
i
eGFP+ cells %
PBS
MBV-Pdl1
ns
Heart
Kidney
Liver
Lung
Spleen
j
PBS
MBV-Pdl1 ****
Indel (%)
Tumor 1
Tumor 2
Tumor 3
Tumor 4
k
Indel (%)
PBS
MBV-Pdl1
ns
heart
kidney
liver
lung
spleen
l
Tumor size (mm3)
PBS
MNP
BV-Pdl1
aPD-L1
MBV-Pdl1
*
**
**
**** ##
Days
m
Survival %
PBS
MNP
BV-Pdl1
aPD-L1
MBV-Pdl1
****
ns
ns
*
Days

Fig. 4. Intratumoral activation of MBV-*Pdl1* suppresses tumor growth. **a**. Schematic of the treatment timeline. **b**. Schematic of intratumoral magnetic activation of MBV. The dimensions and relative positions of the magnets and tumor are drawn to scale. **c**, **d**. Simulated distributions of magnetic flux density (**c**) and magnetic force (**d**) on the tumor surface. Distribution of MBV inside the tumor was assessed by MRI and histological staining. **e**. Representative consecutive MRI cross sections overlaid with computed T_2 relaxivity maps of the tumor. **f**. Representative histological images of tumors treated with PBS or MBV-*Pdl1*. Tumor sections were stained for MNPs by Prussian blue and counterstained with nuclear red. The dashed red circle denotes the needle track. In vivo transduction by MBV was evaluated using MBV-*Pdl1* carrying an eGFP reporter. **g**. Flow cytometry quantification of $eGFP^+$ cells in tumors treated with PBS or MBV-*Pdl1*. **h**. Flow cytometry quantification of $eGFP^+$ cells among cancer cells ($CD44^+$), tumor-associated fibroblast ($ER\text{-}TR7^+$), and immune cells ($CD45^+$) in PBS- or MBV-*Pdl1*-treated tumors. **i**. Flow cytometry quantification of $eGFP^+$ cells in major organs following PBS or MBV-*Pdl1* treatment. **j**. Next-generation sequencing (NGS) quantification of indel frequency in tumors following PBS or MBV-*Pdl1* treatment. **k**. NGS quantification of indel frequency in major organs following PBS or MBV-*Pdl1* treatment. **l**. Tumor volume measured from treatment initiation. Data are presented as mean ± s.e.m. **m**. Kaplan-Meier survival curves following the indicated treatment (n = 8 per group). ns, *, **, ***, and **** denote no significance, $P < 0.05$, $P < 0.01$, $P < 0.001$, and $P < 0.0001$ versus PBS, respectively; ## denote $P < 0.01$ versus anti-PD-L1.

MBV-*Pdl1* remodels the tumor immune microenvironment

Immunostaining confirmed reduced PD-L1 expression in MBV-*Pdl1*-treated tumors but not in BV-*Pdl1*-treated tumors (Fig 5a). Both BV-*Pdl1* and MBV-*Pdl1* treatments increased infiltration of $CD11c^+CD86^+$ dendritic cells (Fig. 5b), whereas MBV-*Pdl1* and aPD-L1 treatment increased $CD3^+CD8^+$ T cell infiltration (Fig. 5c).

To comprehensively characterize the impact of MBV-*Pdl1* on the tumor immune microenvironment, we analyzed $CD45^+$ immune cells isolated from tumors treated with PBS or MBV-*Pdl1*. Flow cytometry analysis revealed a near doubling of $CD45^+$ immune cells in MBV-*Pdl1*-treated tumors relative to PBS controls (Fig. 5d). Single-cell RNA sequencing of tumor-infiltrating immune cells demonstrated marked shift in immune composition following MBV-*Pdl1* treatment (Fig. 5e-g, Supplementary Fig. S16). Tumor treated with PBS were dominated by three major populations – neutrophils, $CD4^+$ T cells, and $CD8^+$ T cells. MBV-*Pdl1* treatment increased immune diversity, with elevated proportions of macrophages,

dendritic cells, B cells, natural killer (NK) cells, accompanied by reduced fractions of neutrophils, and $CD4^+$ T cells.

Antigen-presenting cells, including macrophages, dendritic cells, and B cells, were substantially enriched following MBV-*Pdl1* treatment (Fig. 5g). Dendritic cells increased more than fourfold among $CD45^+$ cells (Fig. 5h), with conventional type 2 dendritic cells (cDC2s) comprising the dominant subset (Fig. 5i, Supplementary Fig. S17a, b). Gene-expression analysis of tumor-infiltrating dendritic cells revealed enrichment of pathways associated with antiviral defense and antitumor immunity, including antigen processing and presentation, activation of innate immune responses, regulation of T cell activation, and type I interferon production (Fig. 5j).

Although the overall proportion of T cells decreased slightly, the $CD8^+/CD4^+$ T cell ratio increased significantly in MBV-*Pdl1*-treated tumors (Fig. 5k, l). Subclustering of $CD8^+$ T cells further revealed a shift from effector and exhausted phenotypes toward naïve and cycling states (Fig. 5m-o). PBS-treated tumors contained higher proportions of effector and exhausted $CD8^+$ T cells, whereas MBV-*Pdl1*-treated tumors exhibited a marked increase in naïve and cycling $CD8^+$ T cells. Consistent with these phenotypes, differential expression analysis showed upregulation of genes associated with proliferation and cytotoxic potential, including *Srm*, *Apex1*, *Xcl1, Gzmc,* and *Cd244a*, alongside reduced expression of inhibitory receptors (*Ctla4*, *Icos*, and *Havcr2*) (Fig. 5p). $CD4^+$ T cell analysis revealed that MBV-*Pdl1* treatment increased memory and regulatory T cells fractions (Supplementary Fig. S17d-f). NK cells were also enriched following MBV-Pdl1 treatment (Fig. 5g). Analysis of exhaustion and inhibitory markers (*Ctla4*, *Cd274*, and *Satb1*) alongside proliferation-associated genes (*Stmn1*, *Mcm3*, *Mcm5*) and activation-associated genes (*Gzmc*, *Ifitm2*, *Apex1*, *C1qbp*) revealed that NK cells in MBV-*Pdl1*-treated tumors exhibited transcriptional signatures consistent with both antiviral activation and antitumor cytotoxicity (Supplementary Fig. S17c).

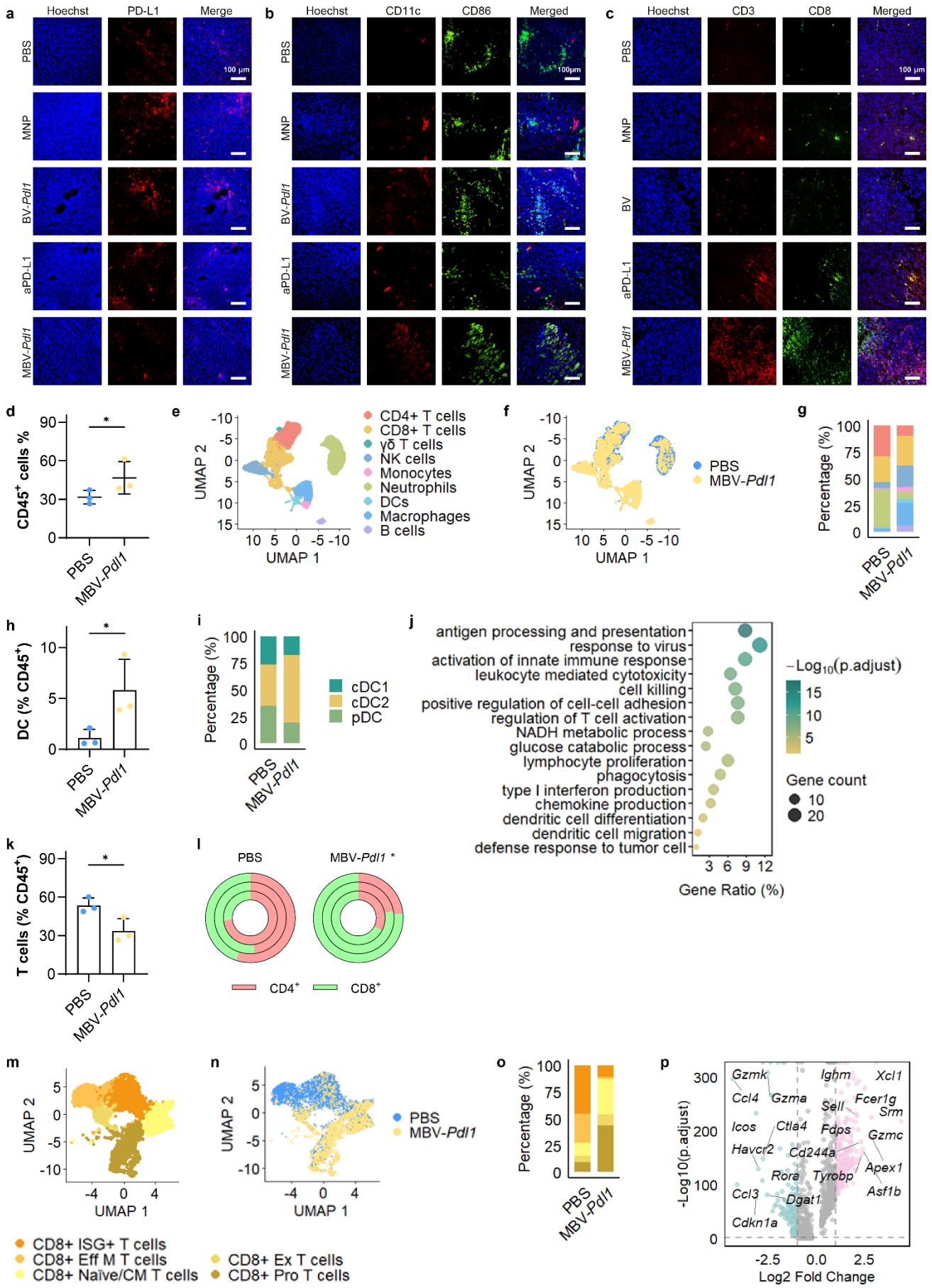
a
Hoechst
PD-L1
Merge
PBS
MNP
BV-Pdl1
aPD-L1
MBV-Pdl1
100 μm
b
Hoechst
CD11c
CD86
Merged
100μm
c
Hoechst
CD3
CD8
Merged
BV
d
CD45+ cells %
PBS
MBV-Pdl1
e
UMAP 2
UMAP 1
CD4+ T cells
CD8+ T cells
γδ T cells
NK cells
Monocytes
Neutrophils
DCs
Macrophages
B cells
f
PBS
MBV-Pdl1
g
Percentage (%)
h
DC (% CD45+)
i
cDC1
cDC2
pDC
j
antigen processing and presentation
response to virus
activation of innate immune response
leukocyte mediated cytotoxicity
cell killing
positive regulation of cell-cell adhesion
regulation of T cell activation
NADH metabolic process
glucose catabolic process
lymphocyte proliferation
phagocytosis
type I interferon production
chemokine production
dendritic cell differentiation
dendritic cell migration
defense response to tumor cell
−Log10(p.adjust)
Gene count
Gene Ratio (%)
k
T cells (% CD45+)
l
PBS
MBV-Pdl1 *
CD4+
CD8+
m
n
o
p
CD8+ ISG+ T cells
CD8+ Eff M T cells
CD8+ Naïve/CM T cells
CD8+ Ex T cells
CD8+ Pro T cells
Gzmk
Ccl4
Gzma
Icos
Ctla4
Havcr2
Cd244a
Rora
Tyrobp
Ccl3
Dgat1
Cdkn1a
Ighm
Xcl1
Sell
Fcer1g
Srm
Fdps
Gzmc
Apex1
Asf1b
-Log10(p.adjust)
Log2 Fold Change

Fig 5. MBV-Pdl1 modulates the tumor immune microenvironment. **a**, **b**, **c**. Representative fluorescence microscopy images of tumors stained for PD-L1 (**a**), dendritic cells ($CD11C^+CD86^+$; **b**), and CD8 T cells ($CD3^+CD8^+$; **c**) following treatment with PBS, MNP, BV-*Pdl1*, anti-PD-L1, or MBV-*Pdl1*. Nuclei were counterstained with Hoechst. **d**. Flow cytometry quantification of $CD45^+$ cells in tumors treated with PBS or MBV-*Pdl1*. The effects of MBV-*Pdl1* treatment on the tumor immune microenvironment were further analyzed by single-cell RNA sequencing (n = 3 per group). **e**. UMAP embedding showing clustering of tumor-infiltrating immune cells. **f**. UMAP showing the distribution of immune cells in PBS- and MBV-*Pdl1*-treated tumors. **g**. Proportions of major immune cell types in PBS- and MBV-*Pdl1*-treated tumors. **h**. Fraction of dendritic cells (DCs) among $CD45^+$ cells in PBS or MBV-*Pdl1*-treated tumors. **i**. Proportions of DC subtypes in PBS- and MBV-*Pdl1*-treated tumors. **j**. Pathway enrichment analysis of DCs in MBV-*Pdl1*-treated tumor relative to PBS. **K**. Fraction of T (γδ, $CD4^+$, and $CD8^+$) cells among $CD45^+$ cells in PBS or MBV-*Pdl1*-treated tumors. **l**. Proportions of $CD4^+$ and $CD8^+$ T cells in PBS and MBV-*Pdl1*-treated tumors; each circle represents one mouse. **m**. UMAP embedding showing clustering of $CD8^+$ T cells. **n**. UMAP showing the distribution of $CD8^+$ T cells in PBS- and MBV-*Pdl1*-treated tumors. **o**. Proportions of $CD8^+$ T cell subtypes in PBS- and MBV-*Pdl1*-treated tumors. **p**. Volcano plot of differentially expressed genes in $CD8^+$ T cells from MBV-*Pdl1*-tumors relative to PBS. * denotes $P < 0.05$ versus PBS. Additional analyses are provided in Supplementary Fig. S17.

MBV-*Pdl1* synergizes with systemic CTLA-4 blockade

To assess compatibility with systemic immune checkpoint blockade, MBV-*Pdl1* was combined with anti-CTLA-4 antibody (aCTLA-4) in MC38 tumor-bearing mice (Fig. 6a). CTLA-4 blockade is a clinically relevant partner for PD1/PD-L1-targeted therapies and can reduce tumor-infiltrating regulatory T cell and attenuate their immunosuppressive activities [44], a feature observed in MBV-*Pdl1* treated tumors. The combination produced greater tumor suppression than either monotherapy or antibody combinations (Fig. 6b-f). Median survival increased to 38 days in the MBV-*Pdl1* + aCTLA-4 group compared with 10 days for PBS, 13.5 days for aCTLA-4 alone, and 14 days for aCTLA-4 + aPD-L1 (Fig. 6g). Two mice in the combination group achieved complete tumor regression. No significant body-weight loss was observed, indicating favorable tolerability (Supplementary Fig. S18).

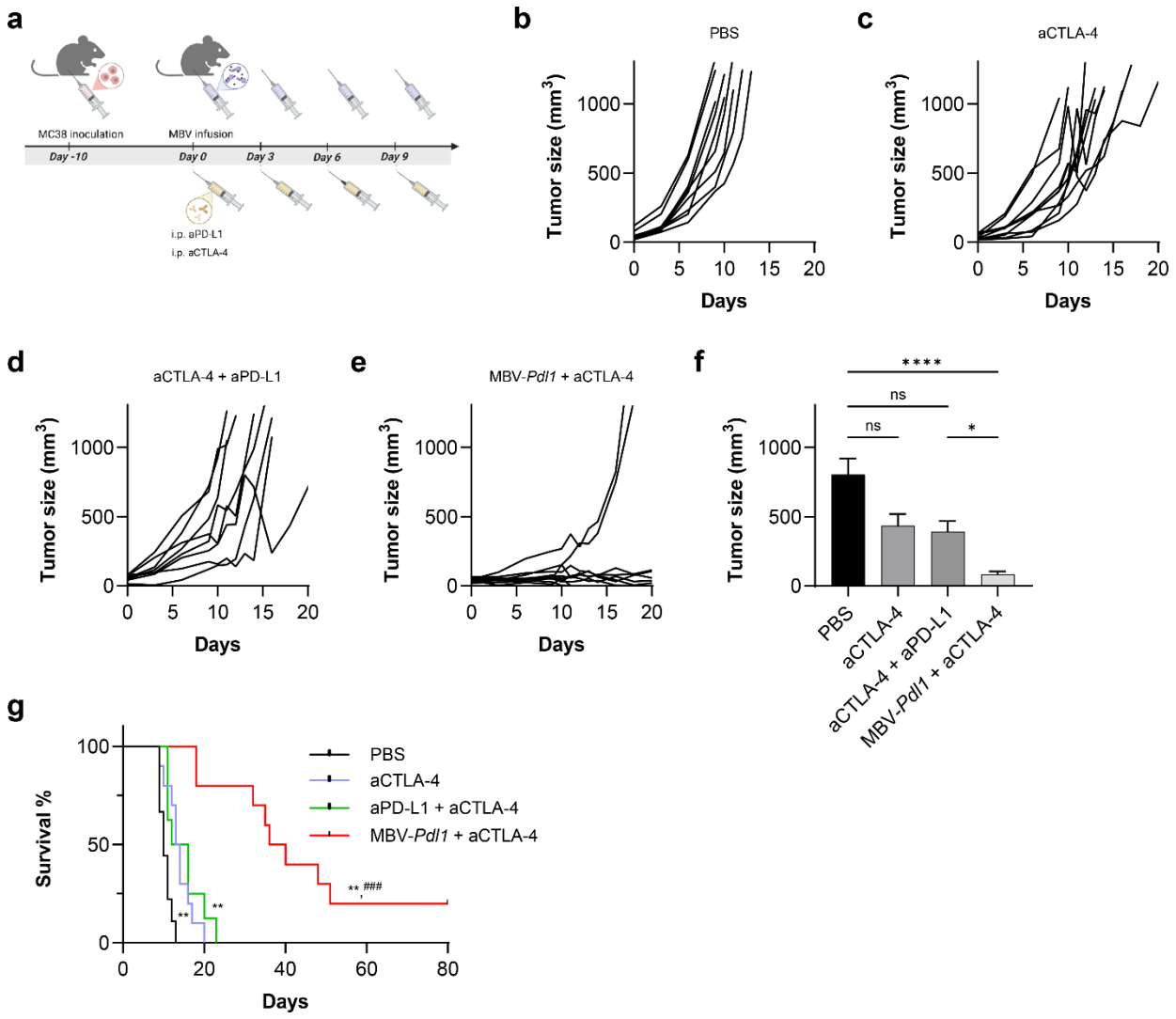

Fig 6. MBV-*Pdl1* and aCTLA-4 synergistically suppress tumor growth. **a**. Schematic of the treatment timeline. **b-e**, Tumor size measured from the initiation of treatment. Data are presented as mean ± s.e.m. **f**. Tumor size measured on day 9 after the initiation of treatment. Data are presented as mean ± s.e.m. ns, *, and **** denote no significance, $P < 0.05$, and $P < 0.0001$, respectively. **g**. Corresponding Kaplan-Meier survival curves following the indicated treatment. ** denotes $P < 0.01$ versus PBS; ### denotes $P < 0.001$ versus anti-PD-L1 + anti-CTLA-4.

Conclusion

Combination immunotherapies aim to overcome tumor immune heterogeneity and adaptive resistance by engaging multiple regulatory pathways, but their effectiveness depends critically on spatial coordination and controlled immune activation. Systemic delivery of immune modulators or genome-editing agents

often lacks this control, increasing the risk of off-target activity and toxicity. The results presented here address this challenge by integrating physical regulation with biologically encoded immune activation to achieve localized immunomodulation within tumors.

We introduce a hybrid nanoplatform that decouples viral immunogenicity from replication by integrating a non-replicating baculoviral vector with magnetic nanoparticles. A defining feature of MBV is the use of orthogonal physical and biological constraints to regulate activity in vivo. Complement sensitivity suppresses off-target viral transduction, while magnetic activation concentrates vector-cell interactions and restores intracellular delivery within the target site. This coupling of an engineered physical on-switch with an endogenous biological off-switch confines viral entry, transgene expression, and CRISPR activity to magnetically targeted tumor regions, reducing risks associated with vector dissemination and prolonged nuclease exposure. Editing is transient at the level of transgene expression but durable at the genomic locus, allowing sustained checkpoint disruption without persistent vector presence.

Baculovirus transduction intrinsically engages antiviral signaling pathways, including interferon responses, chemokine secretion, and antigen-presentation programs, which promote immune-cell recruitment and priming. However, these responses also induce compensatory PD-L1 upregulation that can restrain effector function. Local disruption of *Pdl1* therefore plays an essential role by removing a dominant inhibitory signal while preserving the immunostimulatory context generated by viral sensing. The limited efficacy of tumor-intrinsic PD-L1 knockout alone underscores that therapeutic benefit arises from the coordinated interaction between genome editing and antiviral immune activation rather than checkpoint disruption in isolation.

At the tissue level, MBV-*Pdl1* reshapes the tumor immune microenvironment by increasing immune-cell density and diversity, particularly among antigen-presenting cells. Expansion of dendritic cell populations, together with enhanced antigen-processing and presentation pathways, supports sustained T cell priming

within tumors. The shift in $CD8^+$ T cells toward naïve and cycling states, accompanied by reduced expression of exhaustion-associated genes, is consistent with ongoing recruitment and clonal expansion driven by localized antigen release and cross-presentation. Synergy with systemic CTLA-4 blockade further highlights the importance of coordinating local and systemic immune modulation, integrating complementary mechanisms that operate across distinct spatial scales without overt toxicity.

The modularity of this platform enables extension to other mediators of immune suppression or resistance through programmable genome editing, while the large cargo capacity of baculovirus supports multiplexed guide RNA delivery. Intratumoral infusion of viral vectors has been demonstrated across tumors at diverse anatomic sites [45], and magnetic activation is compatible with deep tissues and is not attenuated by biological barriers [46, 47], supporting translational applicability beyond superficial tumors. At the same time, the requirement for local delivery and external field application imposes practical constraints that will require optimization of injection strategies and magnetic field geometries.

Together, these findings establish MBV as a generalizable framework for spatially confined, genome-editing-based combination immunotherapy that integrates physical control with biologically encoded immune activation. By emphasizing coordination and localization rather than systemic escalation, this approach provides a strategy for coupling genome editing with immune modulation in solid tumors.

Online content

Any methods, additional references, source data, supplementary information, acknowledgements, details of author contributions and competing interests; and statements of data and code availability are available online.

Reference

1. Chen DS, Mellman I. Oncology meets immunology: the cancer-immunity cycle. *Immunity* 2013, **39**(1)**:** 1–10.

2. Binnewies M, Roberts EW, Kersten K, Chan V, Fearon DF, Merad M*, et al.* Understanding the tumor immune microenvironment (TIME) for effective therapy. *Nat Med* 2018, **24**(5)**:** 541–550.

3. Garon EB, Rizvi NA, Hui R, Leighl N, Balmanoukian AS, Eder JP*, et al.* Pembrolizumab for the treatment of non-small-cell lung cancer. *N Engl J Med* 2015, **372**(21)**:** 2018–2028.

4. Hamid O, Robert C, Daud A, Hodi FS, Hwu WJ, Kefford R*, et al.* Safety and tumor responses with lambrolizumab (anti-PD-1) in melanoma. *N Engl J Med* 2013, **369**(2)**:** 134–144.

5. Kalbasi A, Ribas A. Tumour-intrinsic resistance to immune checkpoint blockade. *Nat Rev Immunol* 2020, **20**(1)**:** 25–39.

6. Restifo NP, Smyth MJ, Snyder A. Acquired resistance to immunotherapy and future challenges. *Nat Rev Cancer* 2016, **16**(2)**:** 121–126.

7. Postow MA, Chesney J, Pavlick AC, Robert C, Grossmann K, McDermott D*, et al.* Nivolumab and ipilimumab versus ipilimumab in untreated melanoma. *N Engl J Med* 2015, **372**(21)**:** 2006–2017.

8. Smyth MJ, Ngiow SF, Ribas A, Teng MW. Combination cancer immunotherapies tailored to the tumour microenvironment. *Nat Rev Clin Oncol* 2016, **13**(3)**:** 143–158.

9. Mahoney KM, Rennert PD, Freeman GJ. Combination cancer immunotherapy and new immunomodulatory targets. *Nat Rev Drug Discov* 2015, **14**(8)**:** 561–584.

10. Goswami S, Pauken KE, Wang L, Sharma P. Next-generation combination approaches for immune checkpoint therapy. *Nat Immunol* 2024, **25**(12)**:** 2186–2199.

11. Emens LA, Romero PJ, Anderson AC, Bruno TC, Capitini CM, Collyar D*, et al.* Challenges and opportunities in cancer immunotherapy: a Society for Immunotherapy of Cancer (SITC) strategic vision. *J Immunother Cancer* 2024, **12**(6)**:** e009063.

12. Kim W, Lee S, Kim HS, Song M, Cha YH, Kim Y-H*, et al.* Targeting mutant KRAS with CRISPR-Cas9 controls tumor growth. *Genome Res* 2018, **28**(3)**:** 374–382.

13. Wang P, Zhang L, Xie Y, Wang N, Tang R, Zheng W*, et al.* Genome Editing for Cancer Therapy: Delivery of Cas9 Protein/sgRNA Plasmid via a Gold Nanocluster/Lipid Core-Shell Nanocarrier. *Adv Sci (Weinh)* 2017, **4**(11)**:** 1700175.

14. Chen X, Wang S, Chen Y, Xin H, Zhang S, Wu D*, et al.* Non-invasive activation of intratumoural gene editing for improved adoptive T-cell therapy in solid tumours. *Nat Nanotechnol* 2023, **18**(8)**:** 933–944.

15. Cox DB, Platt RJ, Zhang F. Therapeutic genome editing: prospects and challenges. *Nat Med* 2015, **21**(2)**:** 121–131.

16. Cong L, Ran FA, Cox D, Lin SL, Barretto R, Habib N*, et al.* Multiplex Genome Engineering Using CRISPR/Cas Systems. *Science* 2013, **339**(6121)**:** 819–823.

17. Canver MC, Smith EC, Sher F, Pinello L, Sanjana NE, Shalem O*, et al.* BCL11A enhancer dissection by Cas9-mediated in situ saturating mutagenesis. *Nature* 2015, **527**(7577)**:** 192–197.

18. Tong S, Moyo B, Lee CM, Leong K, Bao G. Engineered materials for in vivo delivery of genome-editing machinery. *Nat Rev Mater* 2019, **4**(11)**:** 726–737.

19. Fu Y, Foden JA, Khayter C, Maeder ML, Reyon D, Joung JK*, et al.* High-frequency off-target mutagenesis induced by CRISPR-Cas nucleases in human cells. *Nat Biotechnol* 2013, **31**(9)**:** 822–826.

20. Hsu PD, Scott DA, Weinstein JA, Ran FA, Konermann S, Agarwala V*, et al.* DNA targeting specificity of RNA-guided Cas9 nucleases. *Nat Biotechnol* 2013, **31**(9)**:** 827–832.

21. Lin YN, Cradick TJ, Brown MT, Deshmukh H, Ranjan P, Sarode N*, et al.* CRISPR/Cas9 systems have off-target activity with insertions or deletions between target DNA and guide RNA sequences. *Nucleic Acids Res* 2014, **42**(11)**:** 7473–7485.

22. Wang Y, Hu JK, Krol A, Li YP, Li CY, Yuan F. Systemic dissemination of viral vectors during intratumoral injection. *Mol Cancer Ther* 2003, **2**(11)**:** 1233–1242.

23. Maeder ML, Stefanidakis M, Wilson CJ, Baral R, Barrera LA, Bounoutas GS*, et al.* Development of a gene-editing approach to restore vision loss in Leber congenital amaurosis type 10. *Nat Med* 2019, **25**(2)**:** 229–233.

24. Airenne KJ, Hu YC, Kost TA, Smith RH, Kotin RM, Ono C*, et al.* Baculovirus: an insect-derived vector for diverse gene transfer applications. *Mol Ther* 2013, **21**(4)**:** 739–749.

25. Kost TA, Condreay JP, Jarvis DL. Baculovirus as versatile vectors for protein expression in insect and mammalian cells. *Nat Biotechnol* 2005, **23**(5)**:** 567–575.

26. Peng R, Zhang S, Cui Y, Shi Y, Gao GF, Qi J. Structures of human-infecting Thogotovirus fusogens support a common ancestor with insect baculovirus. *Proc Natl Acad Sci U S A* 2017, **114**(42)**:** E8905–E8912.

27. Mansouri M, Bellon-Echeverria I, Rizk A, Ehsaei Z, Cianciolo Cosentino C, Silva CS*, et al.* Highly efficient baculovirus-mediated multigene delivery in primary cells. *Nat Commun* 2016, **7:** 11529.

28. Sung L-Y, Chen C-L, Lin S-Y, Li K-C, Yeh C-L, Chen G-Y*, et al.* Efficient gene delivery into cell lines and stem cells using baculovirus. *Nat Protoc* 2014, **9**(8)**:** 1882–1899.

29. Wu C, Wang S. A pH-sensitive heparin-binding sequence from Baculovirus gp64 protein is important for binding to mammalian cells but not to Sf9 insect cells. *J Virol* 2012, **86**(1)**:** 484–491.

30. Ohkawa T, Volkman LE, Welch MD. Actin-based motility drives baculovirus transit to the nucleus and cell surface. *J Cell Biol* 2010, **190**(2)**:** 187–195.

31. Fay N, Pante N. Nuclear entry of DNA viruses. *Front Microbiol* 2015, **6:** 467.

32. Hofmann C, Strauss M. Baculovirus-mediated gene transfer in the presence of human serum or blood facilitated by inhibition of the complement system. *Gene Ther* 1998, **5**(4)**:** 531–536.

33. Zhu H, Zhang L, Tong S, Lee CM, Deshmukh H, Bao G. Spatial control of in vivo CRISPR-Cas9 genome editing via nanomagnets. *Nat Biomed Eng* 2019, **3**(2)**:** 126–136.

34. Abe T, Hemmi H, Miyamoto H, Moriishi K, Tamura S, Takaku H*, et al.* Involvement of the Toll-like receptor 9 signaling pathway in the induction of innate immunity by baculovirus. *J Virol* 2005, **79**(5)**:** 2847–2858.

35. Strauss R, Huser A, Ni S, Tuve S, Kiviat N, Sow PS*, et al.* Baculovirus-based vaccination vectors allow for efficient induction of immune responses against plasmodium falciparum circumsporozoite protein. *Mol Ther* 2007, **15**(1)**:** 193–202.

36. Samson A, Scott KJ, Taggart D, West EJ, Wilson E, Nuovo GJ*, et al.* Intravenous delivery of oncolytic reovirus to brain tumor patients immunologically primes for subsequent checkpoint blockade. *Sci Transl Med* 2018, **10**(422).

37. Garcia-Diaz A, Shin DS, Moreno BH, Saco J, Escuin-Ordinas H, Rodriguez GA*, et al.* Interferon Receptor Signaling Pathways Regulating PD-L1 and PD-L2 Expression. *Cell Rep* 2019, **29**(11)**:** 3766.

38. Evgin L, Huff AL, Wongthida P, Thompson J, Kottke T, Tonne J*, et al.* Oncolytic virus-derived type I interferon restricts CAR T cell therapy. *Nat Commun* 2020, **11**(1)**:** 3187.

39. Tang H, Liang Y, Anders RA, Taube JM, Qiu X, Mulgaonkar A*, et al.* PD-L1 on host cells is essential for PD-L1 blockade-mediated tumor regression. *J Clin Invest* 2018, **128**(2)**:** 580–588.

40. Zhang LL, Tong S, Zhang QB, Bao G. Lipid-Encapsulated Fe_3O_4 Nanoparticles for Multimodal Magnetic Resonance/Fluorescence Imaging. *Acs Appl Nano Mater* 2020, **3**(7)**:** 6785–6797.

41. Michlits G, Jude J, Hinterndorfer M, de Almeida M, Vainorius G, Hubmann M*, et al.* Multilayered VBC score predicts sgRNAs that efficiently generate loss-of-function alleles. *Nat Methods* 2020, **17**(7)**:** 708–716.

42. Nance EA, Woodworth GF, Sailor KA, Shih TY, Xu Q, Swaminathan G*, et al.* A dense poly(ethylene glycol) coating improves penetration of large polymeric nanoparticles within brain tissue. *Sci Transl Med* 2012, **4**(149)**:** 149ra119.

43. Kost TA, Condreay JP. Recombinant baculoviruses as mammalian cell gene-delivery vectors. *Trends Biotechnol* 2002, **20**(4)**:** 173–180.

44. Tanaka A, Sakaguchi S. Regulatory T cells in cancer immunotherapy. *Cell Res* 2017, **27**(1)**:** 109–118.

45. Todo T, Ito H, Ino Y, Ohtsu H, Ota Y, Shibahara J*, et al.* Intratumoral oncolytic herpes virus G47Δ for residual or recurrent glioblastoma: a phase 2 trial. *Nat Med* 2022, **28**(8)**:** 1630–1639.

46. Muthana M, Kennerley AJ, Hughes R, Fagnano E, Richardson J, Paul M*, et al.* Directing cell therapy to anatomic target sites in vivo with magnetic resonance targeting. *Nat Commun* 2015, **6:** 8009.

47. Choi SH, Shin J, Park C, Lee JU, Lee J, Ambo Y*, et al.* In vivo magnetogenetics for cell-type-specific targeting and modulation of brain circuits. *Nat Nanotechnol* 2024, **19**(9)**:** 1333–1343.

Methods

Materials

Iron(III) acetylacetonate (Fe(acac)3, 99.9%), oleic acid (90%), oleylamine (70%), 1,2-tetradecanediol (90%), benzyl ether (99%), chloroform (99%), toluene (99.9%), DMSO (99.9%), ferrozine (97%), were purchased from Sigma-Aldrich. 1,2-Distearoyl-sn-glycero-3-phosphoethanolamine-N-[methoxy (polyethylene glycol)-2000] (DSPE-mPEG$_{2000}$) and 1,2-distearoyl-sn-glycero-3-phosphoethanolamine-N-[maleimide(polyethylene glycol)-2000] (DSPE-PEG$_{2000}$-maleimide) were purchased from Avanti Polar Lipids. Cysteine-terminated TAT peptides (CGYGRKKRRQRRR) were synthesized by Genscript.

Bac-to-Bac baculovirus expression system and Cellfectin II was purchased from Thermo Fisher Scientific. BacPAK qPCR titration kit, NucleoMag® NGS Clean-up and Size Select kit, PrimeScript RT Master Kit, and TB Green Premix Ex Taq Master Mix were purchased from Takara Bio. Plasmids pX330 (catalog no. 42230), pCMV-GFP (catalog no. 11153), and pCMV-iRFP (catalog no. 45457) were obtained from Addgene. All gRNAs (Supplementary Table S1) and PCR primers (Supplementary Table S2, S3, and S4) were synthesized by Eurofins. xGen™ UDI Primers for NGS library preparation were purchased from Integrated DNA Technologies. Quick-DNA™ MicroPrep kit and Quick-RNA Miniprep Kit were purchased from ZYMO Research.

Enzymes, buffers, and kits used for molecular cloning, including Q5® Hot Start High-Fidelity 2× Master Mix, PCR & DNA Cleanup Kit, DNA Gel Extraction Kit, Quick CIP, T4 Polynucleotide Kinase, T4 DNA Ligase Reaction Buffer, BbsI-HF, T7 endonuclease I, and Quick Ligation Kit, were purchased from New England Biolabs. 10-beta competent E. coli cells were also obtained from New England Biolabs.

All antibodies are listed in Supplementary Table S5.

Production of baculoviral vectors

Recombinant baculovirus vectors were generated using the Bac-to-Bac baculovirus expression system. Briefly, the expression cassettes of Cas9, gRNA, and reporter genes were inserted into the pFastBac vector and transformed into DH10Bac competent cells (Supplementary Fig. S2). The recombinant bacmids containing virus genome and the expression cassettes were extracted using the PureLink HiPure Plasmid Miniprep Kit and transfected into Sf9 insect cells using Cellfectin II according to the manufacturer's protocol. The insect cell culture medium containing the budded viruses was centrifuged and filtered to remove cell debris using Bottle Top filters (0.45 μm; Thermo Fisher Scientific). The collected recombinant baculoviral vector was amplified in Sf9 cells for two more passages. Baculoviral stocks at passage 3 was used for all experiments. Viral particles were concentrated and purified by filtration through a 0.45 μm Bottle Top filter followed by centrifugation at 6,000 g for 3 h at 4 °C. The resulting viral pellets were resuspended in PBS and stored at 4 °C until use. Baculoviral titers were quantified using the BacPAK qPCR titration kit.

Synthesis of magnetic nanoparticles

Magnetic nanoparticles (MNPs) were synthesized using a two-step method adapted from previously reported methods [1]. Briefly, magnetite (Fe_3O_4) nanocrystals were prepared by thermal decomposition of iron(III) acetylacetonate ($Fe(acac)_3$) in benzyl ether in the presence of oleic acid, oleylamine, and 1,2-hexadecanediol. To render the nanocrystals water-dispersible, they were coated with a mixture of DSPE-$mPEG_{2000}$ and DSPE-PEG_{2000}-maleimide at a molar ratio of 19:1 using a dual-solvent exchange method [2]. For peptide conjugation, freshly coated MNPs were incubated with cysteine-terminated TAT peptides at a molar ratio of 1:200 in 0.25× PBS overnight at room temperature. Unconjugated peptides were removed by ultracentrifugation at 80,000 g for 35 min at 4°C. The nanoparticles were washed, sterilized by filtration through a 0.22 μm syringe filter, and stored at 4°C until use.

Magnetite nanocrystal size and size distribution of coated MNPs were characterized by transmission electron microscopy (TEM) and dynamic light scattering (DLS). Magnetization curve of nanocrystals was measured at 300K using a superconducting quantum interference device (Quantum Design MPMS). Particle concentrations were quantified using a Ferrozine assay. Successful surface conjugation TAT peptides was confirmed by gel-shift assay (Supplementary Fig. S1).

Cell culture

MC38 murine colon adenocarcinoma cells were obtained from Kerafast, and Sf9 insect cells were obtained from Thermo Fisher Scientific. All cell lines were cultured according to the manufacturers' recommended protocols.

In vitro BV transduction

To evaluate the efficiency and temporal dynamics of BV transduction, MC38 cells were seeded at a density of 4 x 10^4 cells per well in 24-well plates and allowed to adhere overnight. Cells were then incubated with DMEM/F12 containing BV-eGFP at varying multiplicities of infection (MOIs) for 24 h, after which the medium was replaced with fresh DMEM/F12. eGFP expression in MC38 cells were quantified by flow cytometry at the indicated time points.

To assess magnetic activation and complement-mediated inhibition of BV transduction, MC38 cells seeded in 24-well plates were incubated with BV-eGFP in DMEM/F12, BV-eGFP in DMEM/F12 supplemented with 50% adult mouse serum (AMS), or MBV-eGFP in DMEM/F12 supplemented with 50% AMS. For cells treated with MBV-eGFP, culture plates were placed on a custom-designed magnetic plate for 0.5 h to enable magnetic activation (Supplementary Fig. S3). Cells were subsequently washed and maintained in DMEM/F12. eGFP expression in MC38 cells were assessed at 24 h by fluorescence microscopy and flow cytometry. To evaluate magnetic activation of *Pdl1* disruption under complement

pressure, cells were treated with BV-*Pdl1* or MBV-*Pdl1* as described above. eGFP and PD-L1 expression were quantified by flow cytometry at 24 and 48 h post-treatment, respectively.

Design of sgRNAs for *Pdl1* disruption

Six candidate single-guide RNAs (sgRNAs) targeting early exons or key structural regions of *Pdl1* were designed using a bioinformatics pipeline incorporating the Vienna Bioactivity CRISPR score (Supplementary Table S1) [3]. Potential on- and off- target sites were predicted using the CRISPRO web tool (http://crispor.gi.ucsc.edu/crispor.py) [4], and the top four predicted off-target loci for each sgRNA were selected for downstream next generation sequencing (NGS) analysis.

MC38 cells were transfected with pX330-sgRNA plasmid using the jetOPTIMUS transfection reagent. Genomic DNA was harvested 48 h post-transfection using the Quick-DNA™ MicroPrep kit. Genomic regions encompassing CRISPR-Cas9 cleavage sites were amplified by PCR using Q5 Hot Start High-Fidelity 2× Master Mix under the following conditions: initial denaturation at 98 °C for 30 s; 34 cycles of 98 °C for 10 s, 68 °C for 15 s, and 72 °C for 30 s, followed by a final extension at 72°C for 2 min. For T7 endonuclease I (T7E1) assays, mismatched heteroduplex DNA was generated by denaturing and reannealing 1 μg of purified PCR product, followed by digestion with T7 endonuclease I at 37 °C for 1 h. Digestion products were resolved on 2% agarose gels. Gene-modification efficiency was calculated using the formula: $\%\ \text{Gene modification} = 100 * \left(1 - \sqrt{1 - \text{fraction cleaved}}\right)$.

For targeted NGS indel analysis, genomic regions spanning CRISPR-Cas9 cleavage sites were amplified by PCR. PCR amplicons were purified using the NucleoMag® NGS Clean-up and Size Select kit and subsequently indexed using xGen™ UDI 10-nt Primer Plates 1-4 (Integrated DNA Technologies) through a second PCR step (98 °C for 30 s; 30 cycles of 98 °C for 10 s, 64 °C for 15 s, and 72 °C for 30 s; final extension at 72 °C for 2 min). Indexed libraries were purified, verified by 1% agarose gel electrophoresis,

and quantified using a Qubit Fluorometer (Thermo Fisher Scientific). Sequencing was performed on an Illumina MiSeq platform. Indel frequencies and editing profiles were analyzed using CRISPResso2 (http://crispresso2.Pinellolab.org) [5].

In vitro transcriptomic analysis of BV transduction

MC38 cells were transduced with BV-*Pdl1*, MBV-Cas9, or MBV-*Pdl1* for 48 h. Total RNA was isolated using the Quick-RNA Miniprep Kit. Gene-expression profiling was performed using the nCounter® Mouse Tumor Signaling 360™ Panel. Data normalization, differential gene-expression analysis, and pathway enrichment were conducted using the nSolver Analysis Sofeware (v4.0). *P* values in differential gene-expression analysis were adjusted using the Benjamini and Yekutieli method for multiple testing correction.

In vitro characterization of BV-induced immune responses

BV-induced immune responses were evaluated using coculture systems consisting of BV-transduced MC38 cells with either bone marrow-derived dendritic cells (BMDCs) or splenocytes.

To generate BMDC, bone marrow cells were harvested from female C56BL/6 mice and cultured in RPMI-1640 medium supplemented with 10% fetal bovine serum (FBS), 100 U/mL penicillin, 100 μg/mL streptomycin, 1000 U/mL granulocyte-macrophage colony-stimulating factor (GM-CSF), and 800 U/mL interleukin-4 (IL-4) for 3 days. MC38 cells were transduced with BV-*Pdl1* or BV-Cas9 for 24h, after which they were seeded at a density of 2000 cells per well in 96-well plates and allow to adhere overnight. BMDCs were then added to MC38 cells at a ratio of 2:1 (BMDC:MC38). LPS (100 ng/mL) – treated BMDCs were used as a positive control. After an additional 24 h of coculture, total RNA was extracted using the Quick-RNA Miniprep Kit. RNA was reverse transcribed into cDNA using the PrimeScript RT Master Kit. Gene expression was quantified by real-time quantitative PCR (RT-qPCR) using TB Green

Premix Ex Taq Master Mix in a Bio-Rad CFX96 real-time PCR system. Relative gene expression was calculated using the $2^{-\Delta\Delta Ct}$ method.

In parallel experiments, splenocytes were isolated from the spleens of female C57BL/6 mice and cultured in RPMI-1640 medium supplemented with 10% FBS, 100 U/mL penicillin, and 100 μg/mL streptomycin. MC38 cells were transduced with BV for 24 h and subsequently seeded at 2000 cells per well in 96-well plates overnight. Splenocytes were then added at a ratio of 5:1 (splenocytes:MC38). LPS treated splenocytes were used as a positive control. After 24 h of coculture, cytotoxicity was assessed using a Cell Counting Kit-8 (CCK-8) assay. Gene expression was quantified by RT-qPCR as described above.

Design of the magnetic field for intratumoral BV activation.

The magnetic apparatus used for intratumoral BV activation was designed based on magnet availability, tumor dimensions, and simulated magnetic force distribution. The magnetic force exerted on MNPs was calculated using the equation [6]:

$$F = \mu(\boldsymbol{m} \cdot \nabla)\boldsymbol{H}$$

where μ denotes the magnetic permeability of the surrounding tissue, $\boldsymbol{m}$ is the magnetic moment of the MNPs, and $\boldsymbol{H}$ represents the applied magnetic field.

Based on the numerical simulation, four cylindrical NdFeB magnets (N52 grade; K&J Magnetics) were arranged in an alternating polarity configuration to maximize the magnetic field gradient (Supplementary Fig. S9). A custom 3D-printed animal bed was used to reproducibly position tumors at the center of the magnet assay. The resulting magnetic field and force distributions were simulated using a MATLAB program developed in-house.

Magnetically activated *Pdl1* gene disruption in vivo

All animal studies were approved by the Institutional Animal Care and Use Committee at the University of Kentucky. Female C57BL/6 mice (4-5 weeks old) were purchased from Charles River Laboratories. To establish the syngeneic mouse tumor model, mice received a subcutaneous injection of 5×10^5 MC38 cells suspended in 100 μL of PBS into the right flank. Tumor volume and body weight were monitored every 3 days. Tumor volume was calculated using the formula $V = 1/2 \times L \times W^2$, where L and W denote tumor length and width, respectively. Treatments were initiated when tumors reached approximately 50 mm^3. Mouse was euthanized when tumor volume exceeded 1000 mm^3 in accordance with human endpoint guidelines.

In monotherapy studies, mice were randomized into five groups receiving PBS, MNP alone, BV-*Pdl1* alone, MBV-*Pdl1*, or systemic anti-PD-L1 antibody (aPD-L1). MBV-*Pdl1* was prepared by mixing 1.5×10^7 pfu of BV-*Pdl1* with 5 μg of MNP-TAT in 20 μL of PBS. Mice received intratumoral infusion of MBV-*Pdl1* every 3 days for a total of four doses. The injectate was delivered using a fanning technique, in which the needle was partially withdrawn and redirected to facilitate intratumoral distribution. The injection volume was fixed at 0.3 × the tumor volume while maintaining constant vector concentration, and the solutions were infused over approximately 5 min using a syringe pump. For mice treated with MNP alone or BV-*Pdl1* alone, injected doses were matched to the corresponding components in the MBV-*Pdl1* formulation. In the MNP alone or MBV-*Pdl1* groups, mice were positioned laterally on a 3D-printed animal bed immediately following infusion, with tumors aligned within the magnetic field and maintained under anesthesia for 1 h (Supplementary Fig. S9). Systemic aPD-L1 was administered intraperitoneally at a dose of 200 μg in 100 μL PBS on the same dosing schedule.

For combination therapy studies, mice were randomized into four groups receiving PBS, systemic aCTLA-4, systemic aCTLA-4 combined with aPD-L1, or MBV-*Pdl1* combined with systemic aCTLA-4,

administrated every 3 days for a total of four doses. In the aCTLA-4 group, mice received intraperitoneal injection of 200 μg (day 0) or 100 μg (day 3, 6 and 9) of aCTLA-4 in 100 μL PBS [7]. In the aCTLA-4 plus aPD-L1 group, mice received intraperitoneal injection of aCTLA-4 as above and 100 μg aPD-L1 in 100 μL PBS per treatment. In the MBV-*Pdl1* plus aCTLA-4 group, MBV-*Pdl1* was administrated intratumorally as described above, followed by intraperitoneal injection of aCTLA-4 as described above.

Evaluation of in vivo distribution of MBV

To assess the intratumoral distribution of MBV following infusion, tumor-bearing mice received a single intratumoral injection of BV or MBV as described above. In vivo magnetic resonance imaging (MRI) was performed using a 7 T small animal MRI system (PharmaScan, Bruker) equipped with a 38-mm surface coil. Tumors were imaged using a spin-echo sequence with the following parameters: repetition time (TR) = 2,000 ms; echo time (TE) incremented from 12 ms to 144 ms in 12 ms steps; matrix size = 256×256; and field of view (FOV) = 30 mm. T_2 relaxation maps were generated using a custom MATLAB script.

Following MRI, mice were euthanized, and tumors were harvested, cryosectioned, and stained with Prussian blue to visualize intratumoral MNP distribution.

To assess off-target activities of MBV-*Pdl1* in normal tissues, tumor-bearing mice were treated with PBS or MBV-*Pdl1*-eGFP. To minimize underestimation of off-target events resulting from immune clearance of edited cells, MBV-*Pdl1*-eGFP was administrated once at a fourfold dose. 24 h after treatment, mice were euthanized and tumors as well as major organs (heart, kidney, lung, spleen, and liver) were harvested. Each tumor was cut into 4 fragments. Tumor fragments and organs were enzymatically dissociated using an enzyme cocktail (20 μg/mL DNase I, 2 mg/mL Collagenase Type IV, and 0.5 mg/mL Hyaluronidase Type 1-S). Cells were stained with APC-conjugated rat anti-mouse CD45 antibody, PE/Cyanine-conjugated rat anti-mouse/human CD44 antibody, Alexa Fluor 647-conjugated rat anti-mouse/rat/human ER-TR7 antibody and analyzed by flow cytometry.

To assess the *Pdl1* disruption efficiency in the whole tumor, 4 more tumors were harvested 24h after a single injection of MBV-*Pdl1* and minced into 10-12 pieces. Genomic DNA was extracted from mechanically homogenized tissue with a Quick-DNA MicroPrep kit and subjected to targeted NGS amplicon sequencing.

Immunofluorescence staining

To assess PD-L1 expression and dendritic cell and T-cell infiltration, mice were euthanized 3 days after completion of four treatment cycles, and tumors were harvested, fixed in 4% paraformaldehyde on ice for 2 h, and cryosectioned. Tissue sections were treated with 0.3% H_2O_2 for 10 min at room temperature before staining. For PD-L1 detection, sections were incubated with PE-conjugated rat anti-mouse PD-L1 antibody. For visualization of $CD3^+CD8^+$ T cells, sections were blocked with 5% goat serum for 1 h, and incubated with rabbit anti-mouse CD8α antibody for 1 h at room temperature, followed by incubation with Alexa Fluor 594-conjugated rat anti-mouse CD3 antibody and Alexa Fluor 488-conjugated goat anti-rabbit IgG antibody for an additional 1 h. Sections were counterstained with Hoechst 33342 for 5 min at room temperature and mounted using VectaShield Antifade Mounting Media (Vector Laboratories). Similarly, sections were stained for dendrite cells ($CD11c^+CD86^+$). Fluorescence images were acquired using a Nikon Eclipse Ti2 Inverted fluorescence microscope.

Single-cell RNA sequencing

Immunological changes induced by MBV-*Pdl1* were characterized by single-cell RNA sequencing (scRNA-seq) of tumor-infiltrating immune cells isolated from 3 PBS-treated and 3 MBV-*Pdl1*-treated tumors. Two days after the fourth treatment with PBS or MBV-*Pdl1*, mice were euthanized and tumors were harvested for isolation of $CD45^+$ cells following the 10× Genomics Cell Preparation protocol. Tumors were minced into 2-4 mm^3 fragments and enzymatically dissociated using a tumor dissociation

kit (Miltenyi Biotec) for 20 min at 37 °C. Cell suspensions were filtered through a 40-µm cell strainer and centrifuged at 500 g for 7 min at 4 °C. Pellets were resuspended in 2 mL chilled red blood cell lysis buffer and incubated on ice for 3 min, followed by addition of 8 mL RPMI-1640 containing 5% FBS. Cells were filtered through a fresh 40-µm strainer and centrifuged at 500 g for 5 min at 4 °C. Final pellets were resuspended in HBSS supplemented with 5% FBS and labeled with APC-conjugated anti-mouse CD45 antibody for fluorescence-activated cell sorting using a BD FACSymphony™ S6 Cell Sorter. For each tumor, up to 10,000 $CD45^+$ cells were collected and loaded onto a Chromium Controller (10X Genomics) for single-cell encapsulation. Libraries were prepared according to the manufacturer's instructions and sequenced on an Illumina HiSeq 2500 platform.

Raw sequencing data were processed using an R-based pipeline. Gene expression libraries were aligned to the mouse reference genome GRCm39 (10X Genomics pre-built reference, GRCm39-2024-A) using Cell Ranger (v8.0.1). Downstream analyses were performed with Seurat (v5.3.0) [8]. Quality control filtering was applied prior to integration. Cells with ≤ 200 detected genes and genes expressed in fewer than three cells were excluded. Cells with total unique molecular identifier (UMI) counts or numbers of detected genes below the 1st percentile or above the 99th percentile of the respective distributions were removed. Additional filtering excluded cells with ≤ 1,000 UMIs, ≤ 500 detected genes, or ≥ 5% mitochondrial transcript content. Putative doublets were identified and removed using scDblFinder (v1.17.0) with default parameters [9]. After quality control and doublet removal, a total of 30,006 cells were retained for analysis.

Cells from the PBS- and MBV-*Pdl1*-treated tumors were integrated using the harmony (v1.1.0) to correct for batch effects [10]. Principal component analysis (PCA) was performed, and the first 20 Harmony-corrected principal components were used to construct a shared nearest neighbor (SNN) graph. Unsupervised clustering was performed using the Louvain algorithm with a resolution of 1.4. Uniform

Manifold Approximation and Projection (UMAP) was used for visualization. Cell clusters were annotated based on the expression of canonical marker genes. Major immune lineages, including T cells, macrophages, and dendritic cells (DCs), were isolated for independent subclustering analysis. Within each subset, data were renormalized and re-clustered using the same Harmony-based workflow, and subclusters were annotated based on established lineage- and state-specific markers.

Differential gene expression analysis between clusters or experimental groups was performed using the Wilcoxon rank-sum test. Genes with an adjusted p-value < 0.05 and an absolute $\log_2$ fold change ($\log_2$FC) > 0.5 were considered differentially expressed. Gene set enrichment analysis (GSEA) was conducted using the clusterProfiler package (v4.16.0) [11]. Differences in cell-type proportions between experimental groups were assessed using a hypergeometric test.

Statistical analysis

All statistical analyses were performed using GraphPad Prism. Data were analyzed using one-tailed Student's t-test, one-tailed Mann-Whitney test, or one-way analysis of variance (ANOVA) with post-hoc Dunnett's test, unless otherwise specified. Survival data were analyzed using the Log-rank (Mantel-Cox) test. Statistical significance was defined as $P < 0.05$ (* $P < 0.05$; ** $P < 0.01$; *** $P < 0.001$; ns, not significant).

Schematic illustrations

Schematic illustrations were created with Biorender.com.

Reference

1. Zhang LL, Tong S, Zhang QB, Bao G. Lipid-Encapsulated Fe3O4 Nanoparticles for Multimodal Magnetic Resonance/Fluorescence Imaging. *Acs Applied Nano Materials* 2020, **3**(7)**:** 6785–6797.

2. Tong S, Hou S, Ren B, Zheng Z, Bao G. Self-assembly of phospholipid-PEG coating on nanoparticles through dual solvent exchange. *Nano Lett* 2011, **11**(9)**:** 3720–3726.

3. Michlits G, Jude J, Hinterndorfer M, de Almeida M, Vainorius G, Hubmann M*, et al.* Multilayered VBC score predicts sgRNAs that efficiently generate loss-of-function alleles. *Nature methods* 2020, **17**(7)**:** 708–716.

4. Concordet JP, Haeussler M. CRISPOR: intuitive guide selection for CRISPR/Cas9 genome editing experiments and screens. *Nucleic Acids Res* 2018, **46**(W1)**:** W242–W245.

5. Clement K, Rees H, Canver MC, Gehrke JM, Farouni R, Hsu JY*, et al.* CRISPResso2 provides accurate and rapid genome editing sequence analysis. *Nat Biotechnol* 2019, **37**(3)**:** 224–226.

6. Qiu Y, Tong S, Zhang L, Sakurai Y, Myers DR, Hong L*, et al.* Magnetic forces enable controlled drug delivery by disrupting endothelial cell-cell junctions. *Nat Commun* 2017, **8:** 15594.

7. Gao J, Shi LZ, Zhao H, Chen J, Xiong L, He Q*, et al.* Loss of IFN-gamma Pathway Genes in Tumor Cells as a Mechanism of Resistance to Anti-CTLA-4 Therapy. *Cell* 2016, **167**(2)**:** 397–404 e399.

8. Stuart T, Butler A, Hoffman P, Hafemeister C, Papalexi E, Mauck WM, 3rd*, et al.* Comprehensive Integration of Single-Cell Data. *Cell* 2019, **177**(7)**:** 1888–1902 e1821.

9. Germain PL, Lun A, Garcia Meixide C, Macnair W, Robinson MD. Doublet identification in single-cell sequencing data using scDblFinder. *F1000Res* 2021, **10:** 979.

10. Korsunsky I, Millard N, Fan J, Slowikowski K, Zhang F, Wei K*, et al.* Fast, sensitive and accurate integration of single-cell data with Harmony. *Nature methods* 2019, **16**(12)**:** 1289–1296.

11. Xu S, Hu E, Cai Y, Xie Z, Luo X, Zhan L*, et al.* Using clusterProfiler to characterize multiomics data. *Nat Protoc* 2024, **19**(11)**:** 3292–3320.

Data availability

All data and code that support the findings of this study are available from the corresponding author upon reasonable request.

Acknowledgement

This work was supported by the NIH/NIBIB funding (R01EB026893 to S.T.). The authors would like to thank the U.K. Electron Microscopy Center supported by the National Science Foundation (NNCI-2025075), the U.K. Flow Cytometry & Immune Monitoring core facility supported by an NCI Center

Core Support Grant (P30 CA177558), the OncoGenomics Shared Resource Facility of the University of Kentucky Markey Cancer Center (P30CA177558), and the U.K. Bioelectronics and Nanomedicine Research Center Core facility access award (to X.Y.).

Author contributions

X.Y. and S.T. designed the project. X.Y., Z.Y., and S.T. performed the experiments and collected the data. X.Y., L.T., Y.P., J.H., D.H., J.L., C.W., and S.T. performed data analysis. X.Y. and S.T. wrote the original manuscript. X.Y., Y.P., Y.L., and S.T. revised the manuscript. Y.L. and S.T. supervised the project. All authors have given approval to the final version of the manuscript.

Competing interests

X.Y. and S.T. are inventors on a pending, unlicensed patent application assigned to the University of Kentucky and related to the technologies described in this work.

Additional information

Supplementary information The online version contains supplementary material.

Correspondence and requests for materials should be addressed to Sheng Tong.